

The Facile Implementation of Soft/Tunable Multiband Optical Filters by Stacking Vertical Silicon Nanowire Arrays for Smart Sensing

Gil Ju Lee, Yeong Jae Kim, Han Sung Song, Dong Eun Yoo, Dong-Wook Lee, Il-Suk Kang,* and Young Min Song*

Multiple band optical filters for optical smart sensing, which is simultaneous multispectral detection of objects, are intensively used in many applications, such as remote monitoring, biomedical imaging, wearable optical sensors, and wireless communication. Typically, periodically stacked dielectric layers are used in multiple band optical filters. However, the use of dielectrics inevitably results in rigidity and inflexibility, which is not suitable for advanced smart optical sensors fabricated on flexible substrates. Therefore, herein, a strategy to implement soft/tunable multiband optical filters made from silicon nanowire array-based stackable optical filters (Si NW-SOFs) composed of polymeric membranes containing vertical silicon nanowire arrays that filter light from visible to near-infrared regions with a narrow bandwidth is proposed. Theoretical and experimental results indicate wavelength selectivity by geometrical parameters (e.g., diameter, period, and height) and the absence of optical disturbance between the layers in the integrated states. Therefore, multiband optical filters with single- to triple-band stops are easily created by changing Si NW-SOFs. Finally, imaging demonstrations that involve the filtering of monochromatic light sources of three wavelengths (i.e., red, green, and blue) and fluorescent biological tissues show the practical multiple band characteristics of Si NW-SOFs.

observation),^[1–3] biomedical imaging (e.g., fluorescence microscopy and in vivo therapeutics),^[4–6] day/night cameras,^[7,8] color filters,^[9] and optical wireless communications.^[10] Multiple band optical filters have been highlighted as key components in multispectral sensing, but conventional multiband filters are based on tens or more pairs of dielectric materials,^[11,12] which makes them inherently rigid and inflexible. However, their stiff mechanical characteristics are not applicable for the recently developed thin/flexible optical smart sensors, which are fabricated on flexible substrates.^[13–15] In addition, the filtering band cannot be tuned after producing periodically stacked dielectric layers. Also, the recently reported band-tunable filters are limited in reflective filter types.^[16,17]


Herein, we present a pathway for the facile implementation of soft/tunable multiband transmissive optical filters using Si nanowire arrays-based stackable optical filters (Si NW-SOFs) with high wavelength

selectivity and fine/wide bandwidth tunability. Wavelength selectivity results from the HE₁₁ mode of the leaky/guided mode, which is excited even in nanowires with diameters that are a few tens of nanometers and that exhibit diameter dependence (see Supporting Note 1 and Figure S1, Supporting Information, for theoretical details).^[18–22] For fine/wide bandwidth tunability, various stacking combinations of Si NW-SOFs tune the optical filtering band (Figure S2, Supporting Information). Based on these features, we design and fabricate Si NW-SOFs with different geometrical parameters (e.g., diameter, period, and height) using the numerical wave analysis tool and top-down process (see Supporting Information for details). In addition, we spectrally characterize the multiple band features of integrated Si NW-SOFs with single- to triple-band stops. In addition to the spectral results, we experimentally demonstrated the multiband filtering feature of Si NW-SOFs by exposing Si NW-SOFs, which are located on an imaging sensor, to monochromatic light sources of three wavelengths. In addition, we prove that our Si NW-SOFs allow fluorescence tissue imaging by passing fluorescent light and blocking an excitation laser light. Thus, we believe that Si NW-SOFs advance the fields of next-generation

For smart sensing, hyperspectral imaging and/or sensing, which provides information from different spectral domains in a single exposure, have been exploited in several fields such as remote sensing (e.g., vegetative health monitoring and astronomical

G. J. Lee, Y. J. Kim, H. S. Song, Prof. Y. M. Song
School of Electrical Engineering and Computer Science
Gwangju Institute of Science and Technology (GIST)
123 Cheomdangwagi-ro, Buk-gu, Gwangju 61005, Republic of Korea
E-mail: ymsong@gist.ac.kr

D. E. Yoo, D.-W. Lee, Dr. I.-S. Kang
National Nanofab Center
Korea Advanced Institute of Science and Technology
291 Daehak-ro, Yuseong-gu, Daejeon 34141, Republic of Korea
E-mail: iskang@nnfc.re.kr

 The ORCID identification number(s) for the author(s) of this article can be found under <https://doi.org/10.1002/aisy.201900072>.

© 2019 The Authors. Published by WILEY-VCH Verlag GmbH & Co. KGaA, Weinheim. This is an open access article under the terms of the Creative Commons Attribution License, which permits use, distribution and reproduction in any medium, provided the original work is properly cited.

DOI: 10.1002/aisy.201900072

optoelectronics and smart sensors for advanced intelligent systems.

Figure 1a presents the schematic of integrated Si NW-SOFs for multiband filtering. The inset in **Figure 1a** is a photograph that displays yellow and nearly transparent Si NW-SOF layers that have optical resonances in the visible and near-infrared (NIR) ranges, respectively. In addition, the overlapped region shows a nearly yellow color because individual Si NW-SOFs barely influence the other layer. **Figure 1b** depicts the measured transmittance spectra of individual and integrated Si NW-SOFs. This result demonstrates that the inherent resonance characteristics of each layer are maintained when Si NW-SOFs are integrated. **Figure S3**, Supporting Information, shows the structural notations, and the measured Si NW-SOFs have the following geometrical parameters: $D_1 = 100$ nm, $\Lambda_1 = 600$ nm, and $H_1 = 2$ μ m and $D_2 = 160$ nm, $\Lambda_2 = 1250$ nm, and $H_2 = 2$ μ m.

To investigate the effect of the misalignment of the two layers, theoretical simulations are performed as functions of wavelength and displacement (**Figure 1c**). The simulation result demonstrates that the resonant wavelengths, which originate from two Si NW-SOFs, are retained regardless of the displacement.

Figure S4, Supporting Information, explains the displacement and its simulation domain. Electric field simulations demonstrate that this stacking method does not suffer from optical crosstalk between the stacked layers (**Figure 1d**). At a shorter resonant wavelength (500 nm), an electric field is confined only along the interface of the bottom Si nanowires with a shorter diameter (100 nm), whereas at a longer wavelength (850 nm), the strong electric field is localized around the upper Si nanowire with a longer diameter (160 nm). This independence of resonant wavelengths enables the facile implementation of multiple band optical filters.

Furthermore, the stacking of two Si NW-SOFs with resonant wavelengths in both visible ranges allows various color changes, owing to the aforementioned pass bandwidth tuning (**Figure S2**, Supporting Information). **Figure 1e** shows examples of coloration where the bottom and top Si NW-SOFs exhibit yellow (Y) and cyan (C) and magenta (M) and cyan (C) colors, respectively. The geometrical parameters in each Si NW-SOFs are as follows: 1) the yellow Si NW-SOF has $D = 100$ nm/ $\Lambda = 600$ nm/ $H = 2$ μ m, 2) cyan Si NW-SOF has $D = 100$ nm/ $\Lambda = 900$ nm/ $H = 2$ μ m, and 3) magenta Si NW-SOF has $D = 80$ nm/ $\Lambda = 600$ nm/ $H = 2$ μ m.

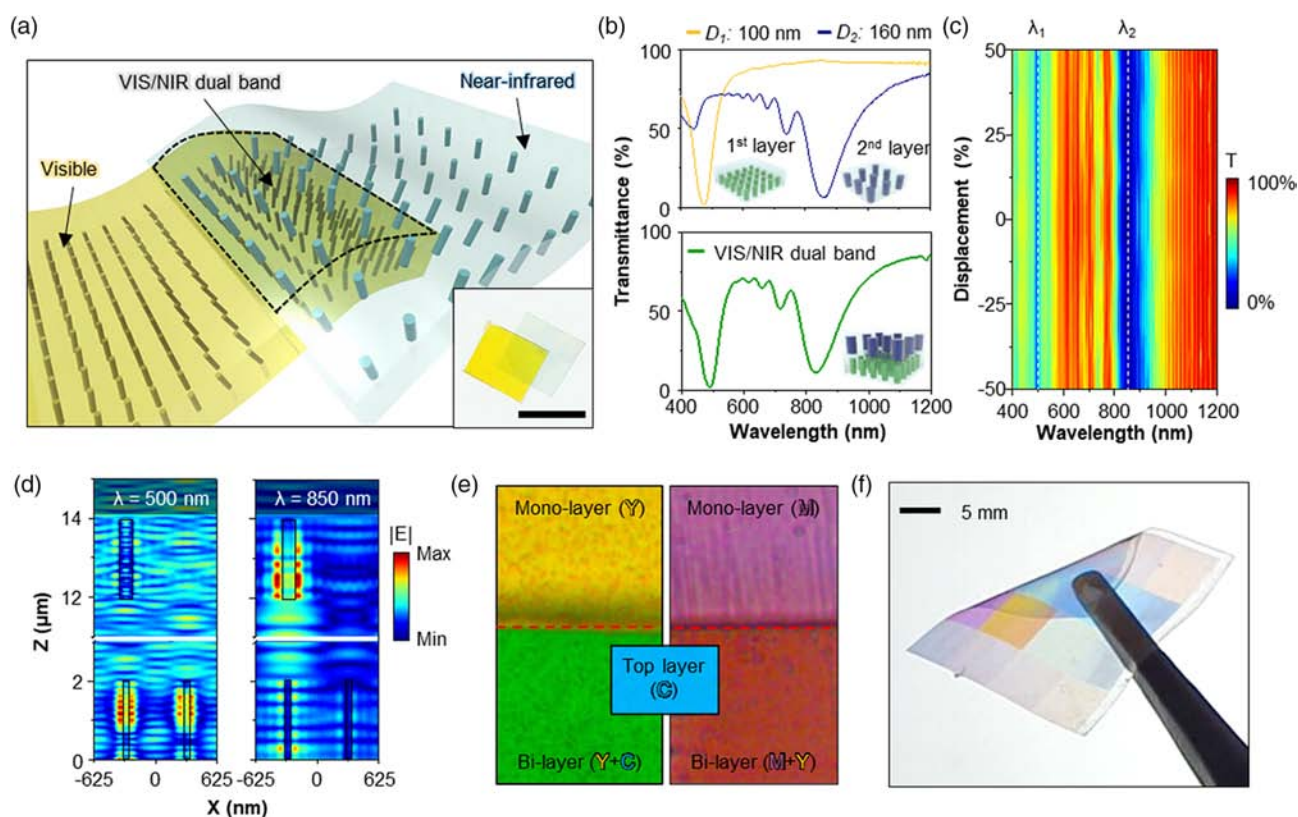


Figure 1. a) Schematic illustration of the Si NW-SOF. The inset shows the Si NW-SOF with resonance in the visible and near-infrared ranges. b) Measured spectra of the (top) individual and (bottom) integrated Si NW-SOFs. In the first layer, the diameter (D_1) and period (Λ_1) are 100 and 600 nm, and the second layer has a 160 nm-diameter (D_2) and a 1250 nm-period (Λ_2). All are 2 μ m high. The detailed structural parameters are presented in **Figure S3**, Supporting Information. c) Calculated transmittance spectra versus the displacement of the first and second layers. The definition of displacement is depicted in **Figure S4**, Supporting Information. d) Simulated electric fields for the aligned state (see **Figure S4**, Supporting Information for details) at the wavelengths of 500 and 850 nm. e) Optical microscopy images of two monolayer Si NW-SOFs, such as (left) yellow (Y) and (right) magenta (M), and bilayer Si NW-SOFs, including (left) yellow + blue (Y + C) and (right) magenta + yellow (M + Y). The center image shows cyan (C)-colored Si NW-SOF. This demonstrates that the Si NW-SOF enables fine coloration by tuning pass band in the visible light range (**Figure S2**, Supporting Information). f) Photograph of the softness of the Si NW-SOF. Changes in the structural parameters, such as diameters and periods, result in color variation.

$\Lambda = 1250 \text{ nm}/H = 2 \mu\text{m}$. The integrated Si NW-SOFs with yellow–cyan and magenta–yellow pairs display green and red colors due to subtractive color mixing because Si NW-SOFs are also subtractive optical filters. Therefore, depending on the application, our Si NW-SOFs can be used as high-purity color filters. In addition to optical characteristics, Si NW-SOFs, which are composed of 1D nanostructures and thin polymers, have remarkable mechanical softness (Figure 1f). The mechanical softness of semiconductor nanowire arrays has been previously studied.^[16,17,23]

Figure 2a shows the simulated and measured spectral properties of Si NW-SOFs as a function of diameter with a 10-nm step. The results of the simulations and measurements are notably coincident and show that the resonant wavelength of Si NW-SOFs is linearly proportional to the diameter, which demonstrates exceptional wavelength selectivity and tunability. As the abovementioned, the resonant wavelengths of Si NW-SOFs

are diameter-dependent excited by leaky/guided waveguide modes of nanowires, particularly the HE_{11} mode, which is dominant in nanowires since it can be allowed even in tiny diameters (a few tens of nanometers). The dispersion relation of the leaky/guided mode shown in Figure S1, Supporting Information, also supports the diameter-dependent resonant feature of simulation and measurement. In addition to the influence of the diameter, other structural parameters, such as period and height, are computationally studied and optimized (Figure S5 and S6, Supporting Information). These results indicate that Si NW-SOFs with a height of $2 \mu\text{m}$ can function effectively. Also, except for a considerably short period exhibiting broadband absorption, excellent filter characteristics are exhibited above the sufficient period (e.g., period $> 600 \text{ nm}$). Based on this optimization process, the fabrication of Si NW-SOFs is conducted via the top-down process depicted in Figure S7 and S8, Supporting Information. The scanning electron microscopy (SEM) images

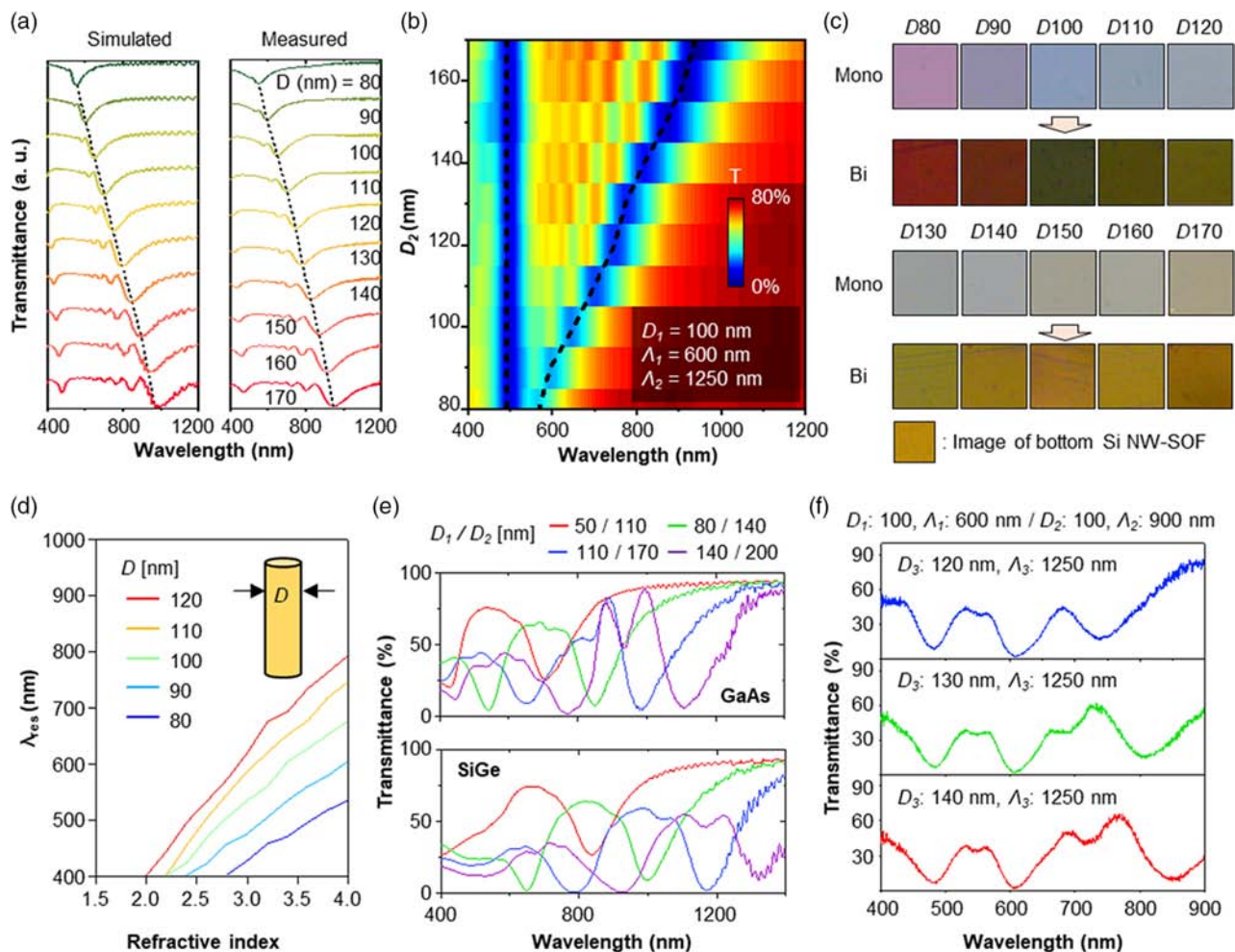


Figure 2. a) Simulated and measured transmittance spectra of Si NW-SOFs with diameters from 80 to 170 nm. b) Contour plot of the measured transmittance spectra of bilayer Si NW-SOFs with different diameters of the top Si NW-SOF. The structural parameters of the measured Si NW-SOFs are as follows: $D_1 = 100 \text{ nm}$, $\Lambda_1 = 600 \text{ nm}$, $\Lambda_2 = 1250 \text{ nm}$, and $H_1 = H_2 = 2000 \text{ nm}$. c) Optical microscopy images of mono- and bilayer Si NW-SOFs. The monolayer Si NW-SOFs and bilayer Si NW-SOFs are presented in Figure 2a,b, respectively. The following inset shows an image of the bottom Si NW-SOF with a period of 600 nm and a diameter of 100 nm . d) Plot of resonant wavelength versus refractive indices of nanowires with five different diameters. e) Simulated spectra of bilayer NW-SOFs composed of different semiconductor materials: GaAs and SiGe. f) Measured spectra of trilayer Si NW-SOFs for the triple-band stop filter.

of the obtained Si nanowire arrays with different diameters and periods are shown in Figure S9 and S10, Supporting Information.

Figure 2b demonstrates the dual-band characteristics of the integrated Si NW-SOFs with a fixed bottom layer (i.e., $D_1 = 100$ nm, $\Lambda_1 = 600$ nm, and $H_1 = 2$ μm) and a top layer with diameters from 80 to 170 nm and a 10-nm step (i.e., $\Lambda_2 = 1250$ nm and $H_2 = 2$). Negligible crosstalk between the top and bottom layers allows outstanding and facile transmitted band tuning. Figure 2c displays the color variation of single-band Si NW-SOFs versus the diameters, and dual-band Si NW-SOFs are presented in Figure 2a,b. Due to the pass bandwidth between two rejection bands, large color changes occur, such as from magenta to red and from blue to green at the diameters of 80 and 100 nm, respectively. At the diameter of 80 nm, the top layer rejects the wavelength of ≈ 550 nm; hence, the reflectance over a wavelength of 600 nm is high. For green, the transmittance between ≈ 500 and ≈ 620 nm is high, and this transmittance peak generates the color green. Above the diameter of 130 nm, the bottom-layer Si NW-SOFs have resonant wavelengths in the NIR

range. Thus, the bottom layer does not contribute to color mixing.

To evaluate the refractive index of nanowires, transmittance simulations are performed for the resonant wavelengths versus refractive indices for five different diameters such as 80, 90, 100, 110, and 120 nm (Figure 2d). As demonstrated earlier, the resonant wavelength becomes longer in proportion to the diameter, whereas the lower the refractive index, the shorter the resonant wavelength. These results suggest that other semiconductor materials could be applied to multiband optical filters instead of Si. To optically investigate NW-SOFs composed of other semiconductors, NW-SOFs of GaAs and SiGe are simulated as the representative examples of other semiconductors (Figure 2e). SiGe has a higher refractive index than GaAs (Figure S11, Supporting Information); thus, the resonant wavelengths of SiGe are longer than those of GaAs. These results demonstrate the universality of nanowire-based multiband optical filters, although the resonant wavelengths can be slightly different depending on the refractive indices. Figure 2f demonstrates the triple-band optical filters produced by integrating three

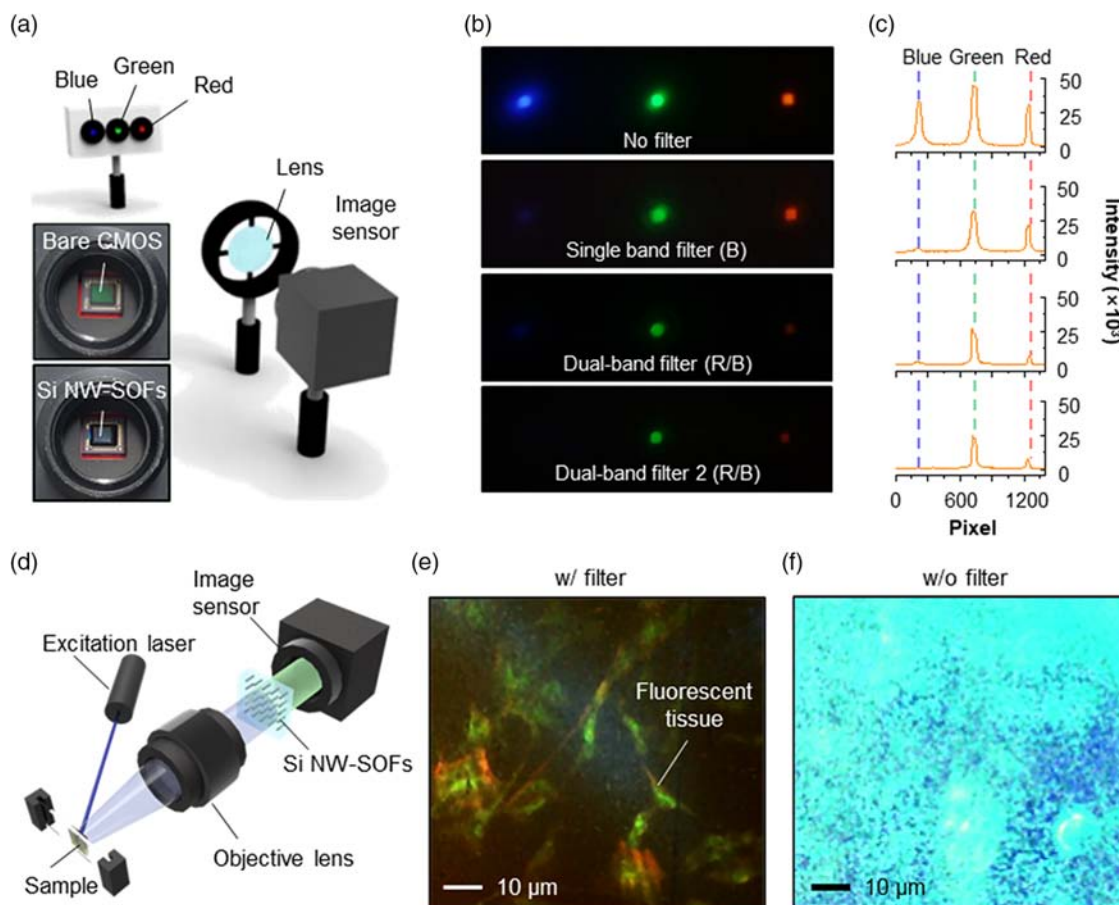


Figure 3. a) Schematic of the measurement setup for multiband filtering of Si NW-SOFs. b) Captured photographs of red, green, and blue light with different Si NW-SOFs without a filter, single-band filter (blue rejection), dual-band filter (blue and red rejection), and dual-band filter 2 (red and blue rejection). The dual-band filter 2 is composed of three layers: one red and two blue stop Si NW-SOFs. c) Cross-sectional intensity plots for each image in Figure 3b. d) Schematic for imaging a fluorescent biosample using Si NW-SOFs. e) Captured image on fluorescence tissue imaging using Si NW-SOFs to reject blue excitation light. f) Captured image of a biosample without Si NW-SOFs. The area with the filter shows clear tissues, whereas the area without the filter displays strong blue light.

different Si NW-SOFs. The first and second layers are fixed as follows: $D_1 = 100$ nm, $\Lambda_1 = 600$ nm, and $H_1 = 2$ μ m and $D_2 = 100$ nm, $\Lambda_2 = 900$ nm, and $H_2 = 2$ μ m. Based on the diameter variation in the third layer, a shift in the resonant wavelength is observed in the NIR range. Furthermore, optical crosstalks between each band are not observed.

In addition to the spectral analyses, the imaging demonstration of Si NW-SOFs should be conducted to evaluate their applicability as multiband filters. To demonstrate the performance of dual-band stop filtering, imaging experiments were performed using monochromatic light sources with center wavelengths of 490, 530, and 590 nm, which emit blue, green, and red colors, respectively (Figure 3a). The detailed setup information is presented in Supporting Information. The Si NW-SOFs are laminated on the cover glass of the complementary metal oxide semiconductor (CMOS) imaging sensor (inset; Figure 3a). Figure 3b,c illustrates the dual-band stop property of stacked Si NW-SOFs. The integrated Si NW-SOFs consist of 490 and 610 nm rejection filters. Without a filter, three monochromatic light sources are clearly captured by the CMOS image sensor, whereas a considerably weak blue light is obtained after attaching Si NW-SOFs with a 490-nm rejection filter. In this image, bright green and red light are still maintained. In the case of dual-band filter 1, both blue and red light are weakly captured, whereas the green light shines brightly. In addition to this double-layer stacking, triple-layer stacking is enabled to reinforce the filtering property at a specific wavelength. Two Si NW-SOFs' filtering at a wavelength of 490 nm and one Si NW-SOF's filtering at a wavelength of 610 nm constitute the dual-band filter 2, as shown in Figure 3b. In the image of the dual-band filter 2, blue light is perfectly eliminated, whereas the green and red light are similar to those observed in the case of dual-band filter 1. These results prove the dual-band filter feature by stacking Si NW-SOFs with different resonant wavelengths.

Using the abovementioned feature of Si NW-SOFs, fluorescence tissue imaging is demonstrated with a customized microscope setup (Figure 3d). Bovine pulmonary artery endothelial (BPAAE) cells with fluorescent substances are used as biological tissues. The detailed information on the tissue and imaging setup is presented in the Supporting Information. A blue wavelength laser excites red and green fluorescence in the tissues. However, this excitation laser light is undesirable in fluorescent imaging. Figure 3e depicts the bilayer Si NW-SOFs with two Si NW-SOFs with blue wavelength rejection. The integrated Si NW-SOFs block the excitation laser light, and thus biological tissues are observed. However, there are no filters to screen the excitation laser light; hence, a clear image of the tissues is not obtained (Figure 3f).

In conclusion, we presented a facile approach to produce soft/tunable multiple band optical filters by stacking Si NW-SOFs with different resonant wavelengths. Using the top-down process, we fabricated various Si nanowire array sets with different diameters (i.e., 80–170 nm in 10-nm steps) and periods (i.e., 600, 900, and 1250 nm). In addition to fabrication, we computationally examined the filtering feature of Si NW-SOFs based on 3D wave analysis. By integrating different Si NW-SOFs, we also spectrally demonstrated multiband filter ranging from the visible to NIR regions. To verify the applicability of Si NW-SOFs, we established customized measurement setups for monochromatic

light imaging and fluorescence biological tissue imaging. In the measurements, we successfully proved the practical multiband stop feature of Si NW-SOFs for different filter combinations. In addition, the universality and expandability of the proposed concept were revealed by the computational study. Therefore, we believe that the proposed Si NW-SOFs can offer a new means for developing small-form and simple multifunctional imaging devices for smart sensing.

Experimental Section

The experimental details, including simulations, fabrication, characterization, measurement setup, and samples, are provided in the Supporting Information.

Supporting Information

Supporting Information is available from the Wiley Online Library or from the author.

Acknowledgements

This research was supported by the National Research Foundation (NRF) of Korea (NRF-2018R1A4A1025623) and by an Institute for Information & Communications Technology Promotion (IITP) grant funded by the Korea government (MSIP) (No.2017000709). This work was also supported by Agency for Defense Development of Korea and Defense Acquisition Program Administration Grant UD170079FD and by GIST Research Institute (GRI) grant funded by the GIST in 2018. G.J.L. acknowledges the support from the NRF (NRF-2017H1A2A1042138).

Conflict of Interest

The authors declare no conflict of interest.

Keywords

multiband optical filters, silicon nanowires, smart sensing, soft/tunable optical filters

Received: July 5, 2019

Revised: August 1, 2019

Published online:

- [1] B. Taruna Widjaja Putra, P. Soni, *Infrared Phys. Technol.* **2017**, *81*, 148.
- [2] J. E. Rhoads, S. Malhotra, P. Scowen, R. Probst, D. McCarthy, *Proc. SPIE* **2010**, *7735*, 77356C.
- [3] J. J. Assmann, J. T. Kerby, A. M. Cunliffe, I. H. Myers-Smith, *J. Unmanned Veh. Syst.* **2019**, *7*, 54.
- [4] J. Bayani, J. Squire, *Curr. Protoc. Cell Biol.* **2004**, *24*, 1.
- [5] J. E. Magnusson, EU patent 1,615,054 A1, **2004**.
- [6] Y. Y. Li, J. J. Chen, H. H. Feng, H. Chen, Q. M. Wang, *Appl. Opt.* **2014**, *53*, 3361.
- [7] A. Toet, M. A. Hogervorst, *SPIE Proc.* **2008**, *6974*, 697402.
- [8] A. Toet, M. A. Hogervorst, R. van Son, J. Dijk, *Int. J. Image Data Fusion* **2011**, *2*, 287.
- [9] X. Liu, G. Fa, Y. Wang, P. Pan, Z. Liu, *IEEE Photonic Technol. Lett.* **2016**, *28*, 9.

- [10] E. Rosenkrantz, S. Arnon, *Opt. Lett.* **2014**, *39*, 4954.
- [11] Y. Cai, S. Zhou, X. Ma, D. Liu, *Appl. Opt.* **2016**, *55*, 9412.
- [12] M. S. Salem, A. M. Abdelaleem, A. A. El-Gamal, M. Amin, *J. Appl. Phys.* **2017**, *121*, 013108.
- [13] Y. M. Song, Y. Xie, V. Malyarchuk, J. Xiao, I. Jung, K.-J. Choi, Z. Liu, H. Park, C. Lu, R.-H. Kim, R. Li, K. B. Crozier, Y. Huang, J. A. Rogers, *Nature* **2013**, *497*, 95.
- [14] C. S. Choi, M. K. Choi, S. Y. Liu, M. S. Kim, O. K. Park, C. K. Im, J. M. Kim, X. L. Qin, G. J. Lee, K. W. Cho, M. B. Kim, E. H. Joh, J. H. Lee, D. H. Son, S. H. Kwon, N. L. Jeon, Y. M. Song, N. S. Lu, D.-H. Kim, *Nat. Commun.* **2017**, *8*, 1664.
- [15] G. J. Lee, C. S. Choi, D.-H. Kim, Y. M. Song, *Adv. Funct. Mater.* **2018**, *28*, 1705202.
- [16] Y. J. Kim, Y. J. Yoo, G. J. Lee, D. E. Yoo, D. W. Lee, V. Siva, H. S. Song, I. S. Kang, and Y. M. Song, *ACS Appl. Mater. Interfaces* **2019**, *11*, 11849.
- [17] H. S. Song, G. J. Lee, D. E. Yoo, Y. J. Kim, Y. J. Yoo, D. W. Lee, V. Siva, I. S. Kang, Y. M. Song, *Sci. Rep.* **2019**, *9*, 3350.
- [18] B. Wang, P. W. Leu, *Opt. Lett.* **2012**, *37*, 3756.
- [19] V. Dagt , N. Anttu, *Nanotechnology* **2018**, *30*, 025710.
- [20] C. Lin, M. L. Povenelli, *Opt. Express* **2009**, *17*, 19371.
- [21] D. R. Abujetas, R. Paniagua-Domínguez, J. A. Sánchez-Gil, *ACS Photonics* **2015**, *2*, 921.
- [22] K. T. Fountaine, W. S. Whitney, H. A. Atwater, *J. Appl. Phys.* **2014**, *116*, 153106.
- [23] P. J. Pauzauskie, P. Yang, *Mater. Today* **2006**, *9*, 36.